

Figure S1. **Additional images of the ultrastructure of *cavin-1*<sup>-/-</sup> whole-muscle sections and isolated muscle fibers.** (A) EM of muscle sections from WT and *cavin-1*<sup>-/-</sup> adult mouse muscle. Note the flat sarcolemmal membrane observed in WT muscle (arrows, top). In contrast, *cavin-1*<sup>-/-</sup> muscle shows a convoluted surface (short arrows, bottom), similar to that observed in isolated muscle fibers (Fig. 1 H) as well as the presence of reticular membrane elements throughout the depth of the muscle fiber (asterisk). Normal triad structure in *cavin-1*<sup>-/-</sup> muscle was also observed (long arrows, bottom). Note the triad connecting to the reticular element (long arrow, bottom right image). (B) EM of ruthenium red-labeled *cavin-1*<sup>-/-</sup> muscle fibers showing reticular elements (indicated by arrows). Bars, 1  $\mu$ m.

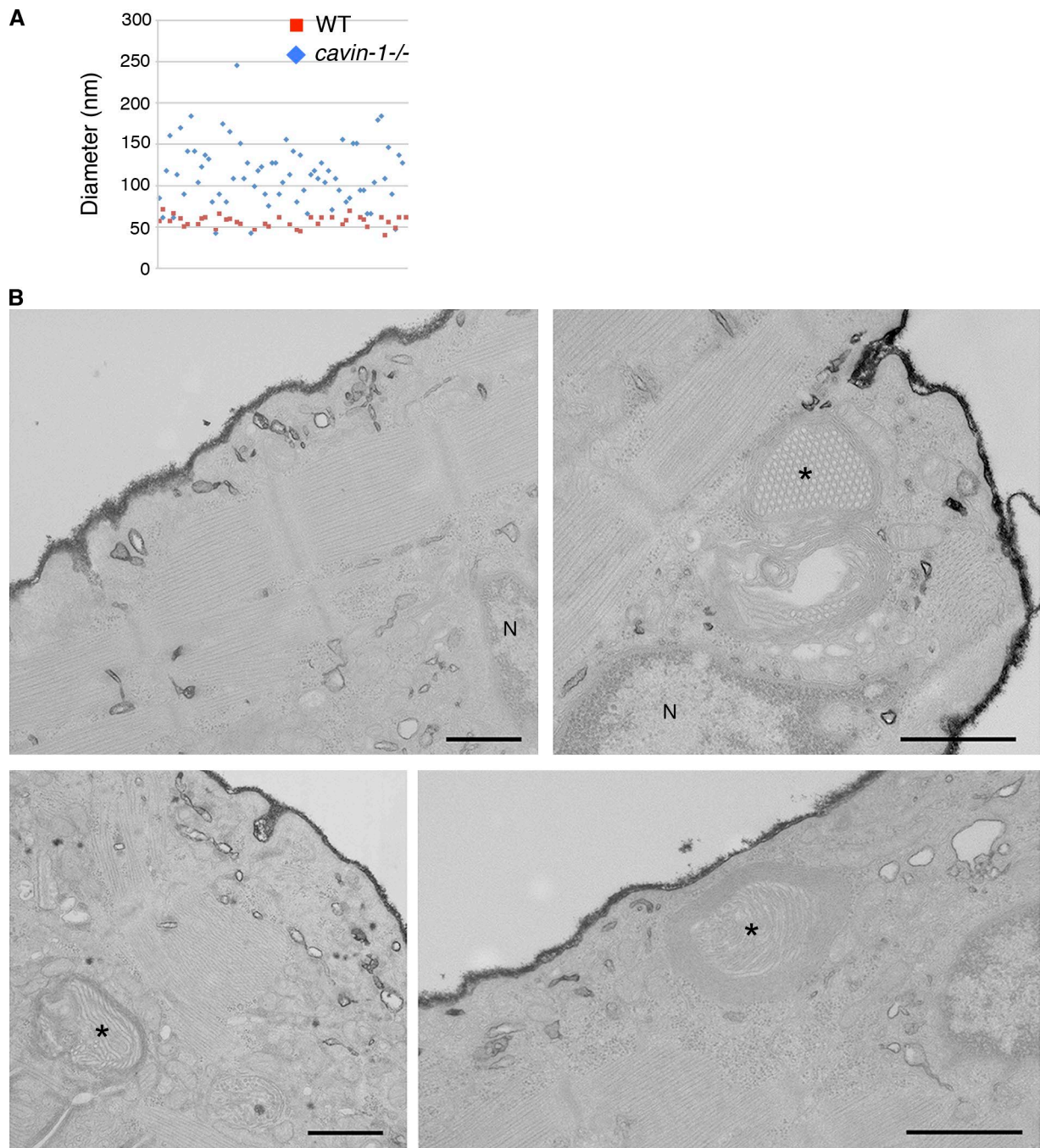


Figure S2. **Mean diameter of caveolae and vacuoles and multilamellar structures in *cavin-1*<sup>-/-</sup> muscle fibers.** (A) Mean diameter measurements of caveolae and vacuoles from WT and *cavin-1*<sup>-/-</sup> muscle fibers, respectively, assuming a spherical form for both structures. Mean diameter of caveolae in WT muscle fibers (red squares) was  $56.7 \pm 1.1$  nm (means  $\pm$  SEM,  $n = 40$ ). Mean diameter of subsarcolemmal vacuoles in *cavin-1*<sup>-/-</sup> muscle fibers (blue diamonds) was  $114.7 \pm 4.5$  nm (means  $\pm$  SEM,  $n = 70$ ). (B) Ultrastructural analysis of ruthenium red-labeled *cavin-1*<sup>-/-</sup> isolated muscle fibers. Images show the convoluted surface of the *cavin-1*<sup>-/-</sup> fibers, with numerous heterogeneous surface-connected elements lying close to the sarcolemma. Note the abundant surface-connected (ruthenium red labeled) large vesicular profiles underlying the sarcolemmal surface and the multilamellar membranous compartments within the cytoplasm (asterisks). Multilamellar structures have been observed in aging male mice (Agbulut et al., 2000); however, we have not observed these structures in any WT muscle used in this study. N, nuclei. Bars, 1  $\mu$ m.



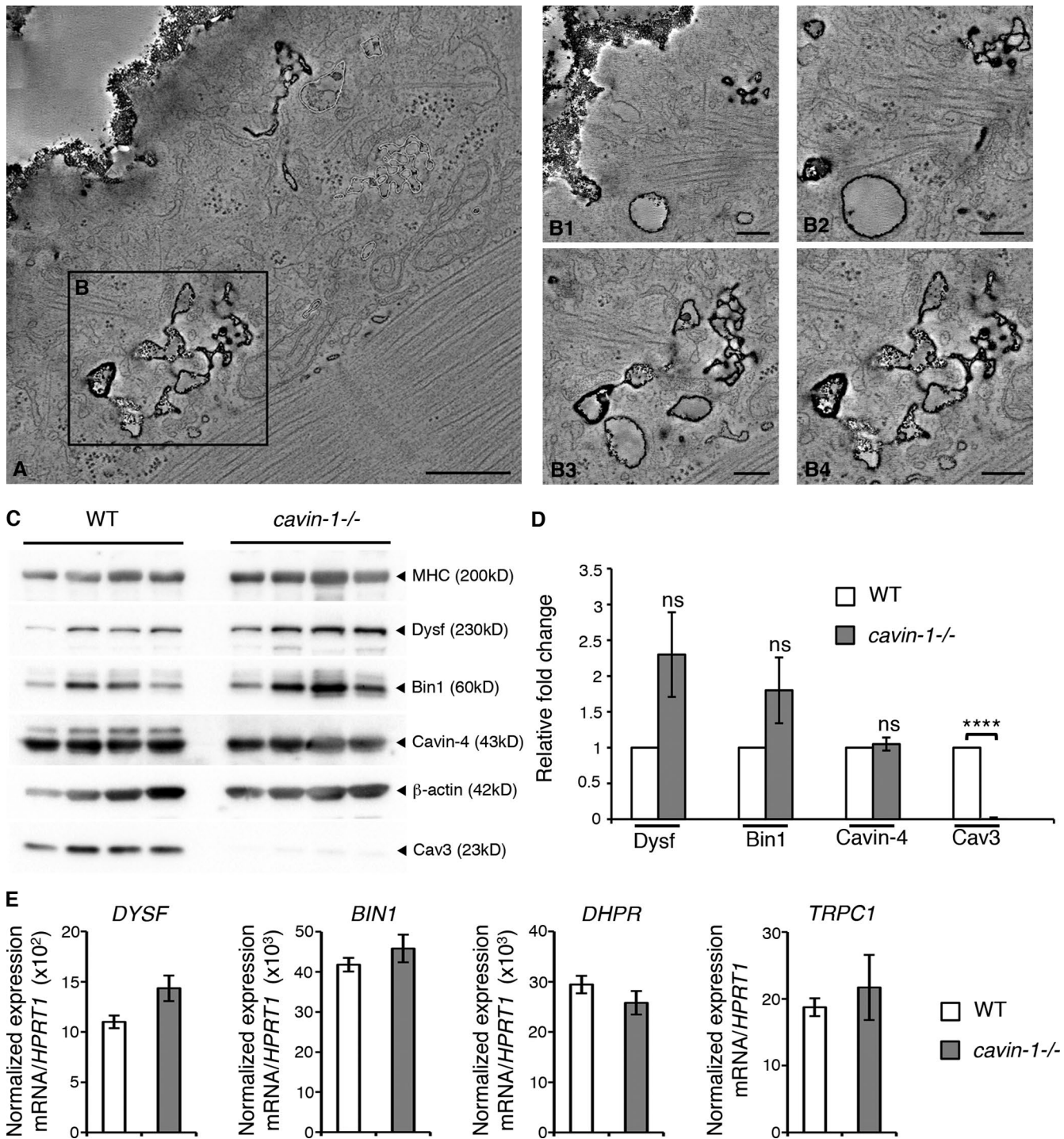
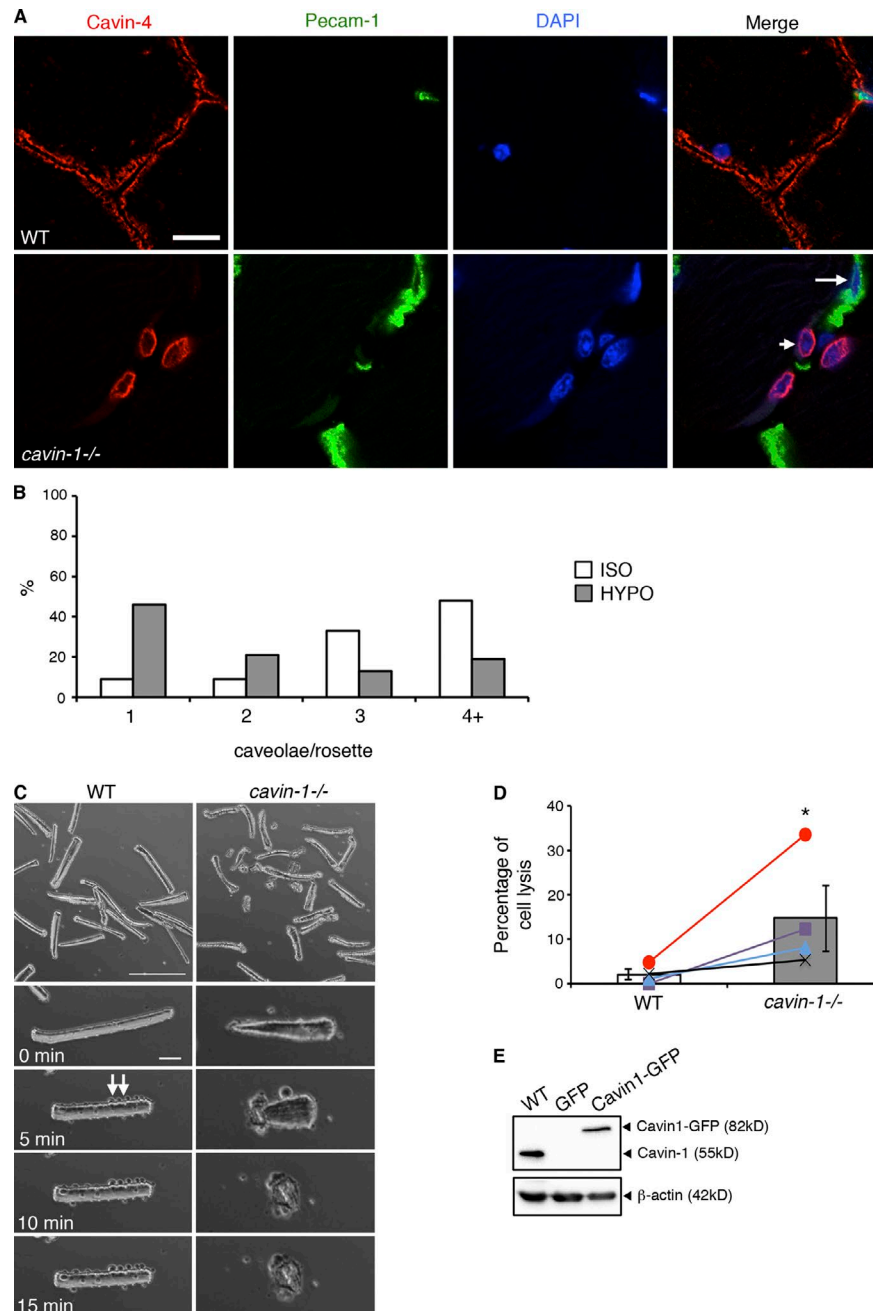


Figure S3. **Additional surface-rendered reconstructions of the honeycomb reticulated networks in *cavin-1*<sup>-/-</sup> muscle fibers and analysis of T-tubule protein expression in WT and *cavin-1*<sup>-/-</sup> muscle.** (A and B) Image in A represents the same tomographic slice of a ruthenium red-labeled *cavin-1*<sup>-/-</sup> muscle fiber as shown in Fig. 3 M. (B) B1–B4 show tomographic slices of ruthenium red-labeled *cavin-1*<sup>-/-</sup> muscle fiber area highlighted in A. Bars: (A) 500 nm; (B1–B4) 200 nm. (C) Western analysis for Dysf, Bin1, Cavin-4, and Cav3 expression in skeletal muscle from four pairs of WT and *cavin-1*<sup>-/-</sup> mice. Myosin heavy chain (MHC) and β-actin expression demonstrate relative muscle protein and total protein loading, respectively. 20 μg of total lysate was loaded. (D) Quantitation of protein expression levels (relative to MHC) in *cavin-1*<sup>-/-</sup> muscle compared with WT muscle. Relative fold change was 2.3 ± 0.6 for Dysf, 1.8 ± 0.5 for Bin1, 1.1 ± 0.2 for Cavin-4, and 0.02 ± 0.0 for Cav3 expression (means ± SEM). \*\*\*\*,  $P \leq 0.0001$ ; ns, not significant. (E) Relative mRNA expression levels of *DYSF*, *BIN1*, *DHPR*, and *TRPC1* (normalized to *HPRT1*) from four pairs of WT and *cavin-1*<sup>-/-</sup> tibialis anterior skeletal muscle. No significant differences were observed.



**Figure S4. Nuclear localization of Cavins in *cavin-1*<sup>-/-</sup> muscle cryosections, electron tomography quantitation of the number of caveolae per rosette after hypo-osmotic treatment, hypo-osmotic treatment of isolated muscle fibers, and relative Cavin-1 expression in WT and Cavin1-GFP-rescued muscle fibers.** (A) Cavin-4/Pecam-1 immunostaining in cryosections of WT and *cavin-1*<sup>-/-</sup> skeletal muscle with DAPI counterstain. In *cavin-1*<sup>-/-</sup> muscle, Cavin-4 localizes to the nucleus (indicated by short arrow). Pecam-1 was used to highlight endothelial cells; no Cavin-4 nuclear labeling was observed in *cavin-1*<sup>-/-</sup> endothelial cells (indicated by long arrow). Bar, 10  $\mu$ m. (B) Quantitation of number of caveolae associated with caveolar rosettes (caveolae/rosette) after incubation in iso-osmotic (ISO) or hypo-osmotic (HYPO) media using electron tomography. 9%, 9%, 33%, and 48% of caveolae from muscle fibers in iso-osmotic media had 1, 2, 3 or greater than 4 (4+) caveolar rosettes, respectively. In contrast, 46%, 21%, 13%, and 19% of caveolae from muscle fibers in hypo-osmotic media had 1, 2, 3, or 4+ caveolar rosettes, respectively. Quantitation was performed on 101 and 67 rosettes from muscle fibers in iso-osmotic and hypo-osmotic media, respectively, and is represented as a percentage of total number of rosettes counted. See Videos 6 and 7. (C) Images in the top row represent WT and *cavin-1*<sup>-/-</sup> muscle fibers in iso-osmotic media. By light microscopy, *cavin-1*<sup>-/-</sup> muscle fibers appear smaller and shorter. We consistently observed a higher proportion of lysed *cavin-1*<sup>-/-</sup> muscle fibers, indicating a general sensitivity to the muscle fiber isolation process; however, these were not included in the quantitation in Fig. S4 D and Fig. 6 R. Time-lapse images of muscle fibers in hypo-osmotic media at 0, 5, 10, and 15 min demonstrate membrane bleb formation (arrows) in WT and *cavin-1*<sup>-/-</sup> muscle fibers. Bar, 500  $\mu$ m. See Video 8. (D) A 15-min incubation in hypo-osmotic media resulted in a sevenfold increase in lysis in *cavin-1*<sup>-/-</sup> muscle fibers in comparison to WT muscle fibers (2.0  $\pm$  1.0% and 14.8  $\pm$  6.4% of lysis in WT and *cavin-1*<sup>-/-</sup> muscle fibers, respectively). Percentage of cell lysis was determined by counting the survival of 401 and 508 muscle fibers from four pairs of WT and *cavin-1*<sup>-/-</sup> mice, respectively. Dot plots represent individual results of the four pairs of mice; note that the percentage of cell lysis is consistently higher in the absence of Cavin-1. Error bars show means  $\pm$  SEM. \*,  $P \leq 0.05$ . (E) Western analysis of FDB muscle from WT mice and *cavin-1*<sup>-/-</sup> mice expressing GFP or Cavin1-GFP. Blot was probed with the anti-Cavin-1 antibody to demonstrate relative expression levels of exogenous Cavin1-GFP to endogenous WT Cavin-1 (representative image based on 50–80% transduction efficiency of muscle fibers).  $\beta$ -Actin demonstrates total protein loading. 50  $\mu$ g of total protein lysate was loaded.

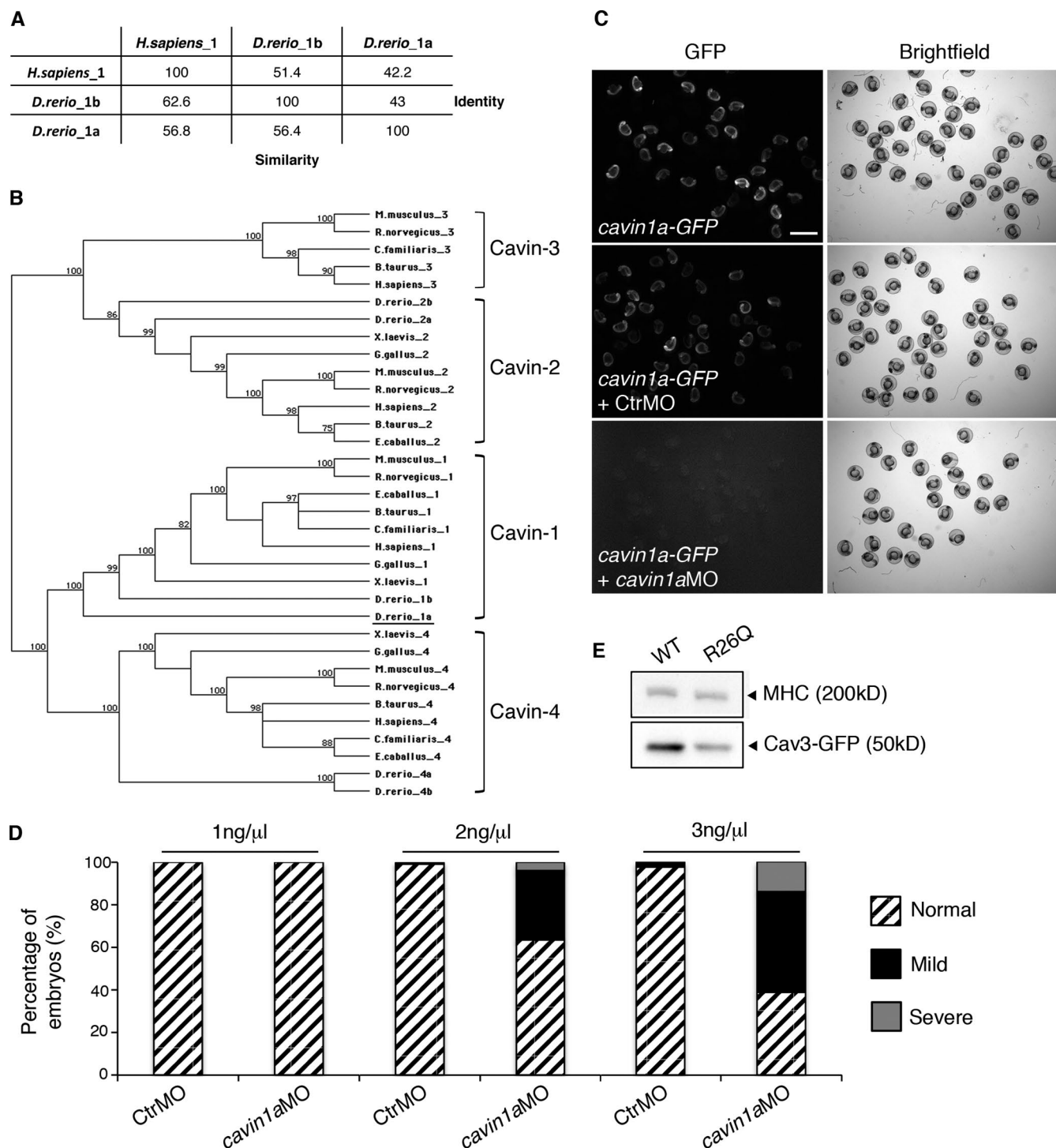
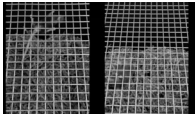
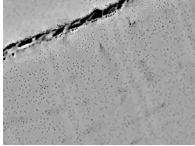


Figure S5. **Evolutionary analysis for *D. rerio* Cavin-1a, additional controls and dose-response graph for MO injections, and Western analysis of Cav3-GFP expression in zebrafish embryos.** (A) Percentage identity/similarity of *D. rerio* Cavin-1a to *Homo sapiens* Cavin-1 and *D. rerio* Cavin-1b. (B) Evolutionary analysis of Cavins 1–4 from cow (*Bos taurus*), dog (*Canis familiaris*), zebrafish (*D. rerio*), horse (*Equus caballus*), chicken (*Gallus gallus*), human (*H. sapiens*), mouse (*Mus musculus*), rat (*Rattus norvegicus*), and frog (*Xenopus laevis*). Numbers represent the percentage of 1,000 bootstrap trials that supports the branch. Cavin-1a is underlined. (C) Embryos were injected with *cavin1a*-GFP mRNA, which includes the *cavin1a* MO target sequence, or coinjected with *cavin1a*-GFP mRNA and either control (CtrMO) or *cavin1a* morpholino (*cavin1a*MO). Embryos were imaged at 24 hpf; left images show GFP fluorescence, and right images show corresponding brightfield image. Bar, 500  $\mu$ m. (D) Dose-response curve for *cavin1a* MO injection. WT zebrafish embryos were injected with increasing concentrations of control MO or *cavin1a*MO and live embryos scored at 72 hpf. Morphant phenotypes were classified into groups of normal, mild with cardiac edema, or severely affected morphants (as shown in Fig. 7 C). Quantitation was performed on a minimum of two clutches per MO concentration. (E) Western analysis of Cav3-WT-GFP (WT) and Cav3-R26Q-GFP zebrafish embryos using anti-GFP antibody. Myosin heavy chain (MHC) expression demonstrates relative protein loading. 50  $\mu$ g of protein lysate was loaded.

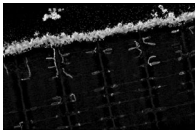




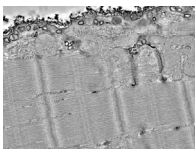
Video 1. **Four-limb hang test in WT and *cavin-1*<sup>-/-</sup> mice.** This video demonstrates the set up for the four-limb hang test used on WT (left) and *cavin-1*<sup>-/-</sup> (right) mice. Mice were required to grip an inverted mesh screen; the total length of time (minutes) that each mouse could grip the screen was recorded.



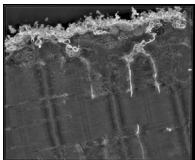
Video 2. **EM tomogram of a WT muscle fiber.** Isolated muscle fibers were fixed in the presence of ruthenium red. 300-nm sections were cut, and dual-axis tilt series data were collected over a tilt range of  $\pm 66^\circ$  at  $1.5^\circ$  increments and reconstructed with the R-weighted back projection algorithm using IMOD/Etomo software. Video is displayed at 30 frames/s.



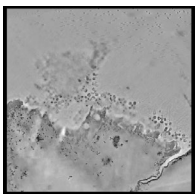
Video 3. **3D representation of a WT muscle fiber.** Isolated muscle fibers were fixed in the presence of ruthenium red. 300-nm sections were cut and dual-axis tilt series data were collected over a tilt range of  $\pm 66^\circ$  at  $1.5^\circ$  increments and reconstructed with the R-weighted back projection algorithm using IMOD/Etomo software. A 3D representation of the WT muscle fiber was generated using the UCSF Chimera software package. Video is displayed at 30 frames/s.



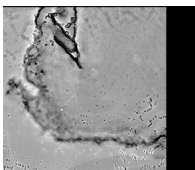
Video 4. **EM tomogram of a *cavin-1*<sup>-/-</sup> muscle fiber.** Isolated muscle fibers were fixed in the presence of ruthenium red. 300-nm sections were cut, and dual-axis tilt series data were collected over a tilt range of  $\pm 66^\circ$  at  $1.5^\circ$  increments and reconstructed with the R-weighted back projection algorithm using IMOD/Etomo software. Video is displayed at 30 frames/s.



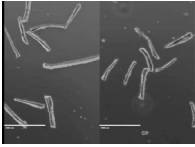
Video 5. **3D representation of a *cavin-1*<sup>-/-</sup> muscle fiber.** Isolated muscle fibers were fixed in the presence of ruthenium red. 300-nm sections were cut, and dual-axis tilt series data were collected over a tilt range of  $\pm 66^\circ$  at  $1.5^\circ$  increments and reconstructed with the R-weighted back projection algorithm using IMOD/Etomo software. A 3D representation of the *cavin-1*<sup>-/-</sup> muscle fiber shown in Video 4 was generated using the UCSF Chimera software package. Video is displayed at 30 frames/s.



Video 6. **EM tomogram of a WT muscle fiber in iso-osmotic media.** WT muscle fibers were isolated, incubated in iso-osmotic (growth) medium, and fixed in the presence of ruthenium red. 300-nm sections were cut, and dual-axis tilt series data were collected over a tilt range of  $\pm 66^\circ$  at  $1.5^\circ$  increments and reconstructed with the R-weighted back projection algorithm using IMOD/Etomo software. The video shows isosurface rendering of a WT muscle fiber (with surface-connected caveolar rosettes highlighted in yellow) after incubation in an iso-osmotic medium. Video is displayed at 6 frames/s.



Video 7. **EM tomogram of a WT muscle fiber in hypo-osmotic media.** WT muscle fibers were isolated, incubated in a hypo-osmotic medium for 15 min, and fixed in the presence of ruthenium red. 300-nm sections were cut, and dual-axis tilt series data were collected over a tilt range of  $\pm 66^\circ$  at  $1.5^\circ$  increments and reconstructed with the R-weighted back projection algorithm using IMOD/Etomo software. The video shows an EM tomogram of a WT muscle fiber (with the remaining, predominantly single, caveolae highlighted by colored circles using a scatter point model) after incubation in a hypo-osmotic medium. Video is displayed at 10 frames/s.



Video 8. **Time lapse of WT and *cavin-1*<sup>-/-</sup> muscle fibers in a hypo-osmotic medium.** Isolated muscle fibers from WT (left) and *cavin-1*<sup>-/-</sup> (right) mice were incubated in a hypo-osmotic medium for 15 min. Images were captured on an EVOSfl microscope using a 4× objective under phase contrast, with one image taken every 15 s over the 15-min period. Video is displayed at 30 frames/s. Bar, 1,000 μm.

## Reference

Agbulut, O., J. Destombes, D. Thiesson, and G. Butler-Browne. 2000. Age-related appearance of tubular aggregates in the skeletal muscle of almost all male inbred mice. *Histochem. Cell Biol.* 114:477–481.